ICARUS **128,** 241–249 (1997)
ARTICLE NO. IS975738

Dynamics of Distant Moons of Asteroids

Douglas P. Hamilton

Astronomy Department, University of Maryland, College Park, Maryland 20742–2421
E-mail: hamilton@astro.umd.edu

and

Alexander V. Krivov

Astronomical Institute, St. Petersburg University, St. Petersburg, Russia

Received October 7, 1996; revised March 24, 1997

We introduce a new analytic method for treating the orbital motions of objects about asteroids and planets. For an asteroid following a circular path around the Sun, we rewrite Jacobi's integral of the motion in terms of the orbital elements relative to the asteroid. This procedure is similar to the derivation of Tisserand's Constant, but here we make the approximation that the satellite is bound to the asteroid rather than far from it. In addition, we retain high order terms that Tisserand ignored and make no assumptions about the relative masses of the asteroid and its satellite. We then average our expression over one circuit of the binary asteroid about its center of mass and obtain the "Generalized Tisserand Constant." We use the Generalized Tisserand Constant to elucidate properties of distant orbits and test our predictions against numerical integrations. In particular, we show analytically that planar prograde orbits are elongated along the Sun–asteroid line, that planar retrograde orbits extend furthest perpendicular to the Sun–asteroid line, and that retrograde orbits are more stable than prograde ones. Our formalism can be extended (i) to three dimensions and (ii) to apply to faint dusty rings around planets by including the effects of planetary oblateness, radiation pressure, and the electromagnetic force from a rotating dipolar magnetic field.

1. INTRODUCTION

The unexpected discovery of Dactyl, a moon with radius ≈0.75 km orbiting the asteroid Ida, suggests that binary asteroids may be quite common and has led to renewed interest in the orbital dynamics of asteroidal satellites. Several recent studies have investigated orbits of a test mass near an irregular, rotating asteroid where a highly nonspherical gravity field determines orbital motions (Geissler *et al.* 1995, Scheeres 1994, Scheeres *et al.* 1996). Here we instead focus on relatively distant orbits where the influence of an asteroid's asymmetric gravity field is small and solar perturbations dominate. Since the detailed mass distribution within the asteroid is relatively unimportant in this regime, orbits about one asteroid are similar to those about another as long as the eccentricities of the asteroidal orbits do not differ greatly.

In this paper, we investigate two distinct types of orbits—prograde and retrograde—in which the Sun, asteroid, and asteroidal satellite all move within a fixed plane. Prograde orbits are those for which the angular momentum vectors of the satellite's motion about the asteroid and the asteroid's motion around the Sun are parallel; for retrograde orbits, these vectors are antiparallel. Several numerical studies have focused on the differences between prograde and retrograde orbits and found the latter are more stable than the former (for historical references, consult Szebehely 1978; for more recent work see, e.g. Innanen 1979, Huang and Innanen 1983, Zhang and Innanen 1988, Chauvineau and Mignard 1990a, 1990b, and Hamilton and Burns 1991). Approximate analytic escape criteria have been derived, most of which follow from considerations of the Jacobi constant (e.g. Szebehely 1978, and Markellos and Roy 1981) or equating forces in a rotating frame (e.g. King 1962, Innanen 1979). Interestingly, all previous estimates which made use of the Jacobi constant show that, with increasing orbital size, retrograde orbits are energetically able to escape *before* prograde orbits despite the fact that retrograde orbits are numerically observed to be *more* stable. Here we resolve this apparent paradox by deriving a Generalized Tisserand Constant from Jacobi's Integral, and using it to show analytically that prograde orbits are indeed less stable than retrograde orbits. Our purpose is not to derive a highly accurate orbital theory (e.g. Brown and Shook 1933, Murray and Harper 1993), but rather to elucidate the differences between prograde and retrograde orbits about asteroids and planets with a simple analytical

0019-1035/97 $25.00

argument. In the next sections, we first derive the Generalized Tisserand Constant and then use it to investigate basic properties of distant orbits.

2. GENERALIZED TISSERAND CONSTANT

The three body problem of celestial mechanics, for which no general analytic solution exists, has been extensively studied and classified into several subproblems. One of these, the *restricted three body problem*, concerns the motion of an (assumed massless) particle in the gravitational fields of two massive objects. The two large objects are uninfluenced by the massless particle and hence move along Keplerian orbits; these orbits are circles in the *circular restricted three body problem*. Although there is no general solution for the circular restricted three body problem either, an integral of the motion known as Jacobi's integral or Jacobi's constant does exist. Jacobi's integral is normally written as a function of the coordinates (x_{cm}, y_{cm}) of the massless body measured in a reference frame with its origin at the center of mass of the system (nearly the center of the Sun for the Sun–asteroid system which we consider) and rotating with the constant angular velocity $n_\odot$ of the circular orbits. In this frame, Jacobi's integral has the form (Danby 1988):

$$C_\odot = \frac{2GM_\odot}{r_\odot} + \frac{2GM}{r} + n_\odot^2(x_{cm}^2 + y_{cm}^2) - v_{cm}^2, \qquad (1)$$

where G is the gravitational constant, $M_\odot$ and M are the solar and asteroidal masses, and $r_\odot$ and r are the distances from the third body to the Sun and to the asteroid, respectively. The coordinate x_{cm} is measured along the Sun–asteroid line, the coordinate y_{cm} is perpendicular to this line and in the plane of the asteroid's orbit, and v_{cm} is the speed of the massless object in the rotating reference frame. The total orbital energy measured in the rotating frame is given by $-C_\odot/2$, where $C_\odot$ is Jacobi's constant. If the coordinates of the massless body are eliminated in favor of its orbital elements one obtains, after assuming $M \ll M_\odot$ and large r, Tisserand's Constant,

$$C_\odot = \frac{GM_\odot}{a_\odot} + 2n_\odot^2 R^2 \left(\frac{a_\odot}{R}\right)^{1/2} (1 - e_\odot^2)^{1/2} \cos(i_\odot). \qquad (2)$$

Here $a_\odot$, $e_\odot$, $i_\odot$ are the heliocentric semimajor axis, eccentricity, and inclination of the massless body, respectively, and R is the Sun–asteroid distance. Tisserand originally considered the Sun–Jupiter–comet problem and applied Eq. (2) to identify comets which had suffered gravitational interactions with Jupiter. Tisserand's Constant includes the effects of solar gravity on the assumed massless comet but ignores the gravity of Jupiter (note that only the solar mass appears in Eq. (2)), which is an excellent approximation as long as the comet is far from the planet. For the current application to distant circumasteroidal orbits, however, gravity from both the Sun and the asteroid is important and, moreover, that of the asteroid dominates. We must, therefore, extend Tisserand's Constant by including both asteroidal and solar gravity.

This is accomplished by first transforming Jacobi's integral from Sun-centered to asteroid-centered coordinates (e.g., Chauvineau and Mignard 1990a, Hamilton and Burns 1991) since the asteroid's gravity is the dominant force. We simplify the integral by taking only the first-order perturbation term due to solar gravity, the so-called "tidal term" rather than the full expression. This step is *Hill's approximation*; it assumes that the asteroid–satellite distance is much less than the asteroid–Sun distance which is an excellent approximation for all bound asteroidal satellites. Hill's approximation also assumes that one mass (the Sun) is large compared to the other two (the binary asteroid), while the circular restricted approximation assumes that one mass (the asteroidal satellite) is small compared to the other two (the Sun and the asteroid); these approximations are independent cases of the full three body problem (e.g. Hénon and Petit 1986). As we are using Hill's approximation, the following results apply to binary asteroids with arbitrary mass ratios; in particular, the satellite's mass need not be small compared to the asteroid's. Transforming Jacobi's integral, we find (Hamilton and Burns 1991) that

$$C = \frac{2GM}{r} + n_\odot^2(3x^2 - z^2) - v^2, \qquad (3)$$

where $n_\odot = (GM_\odot/R^3)^{1/2}$ is the mean motion of the asteroid about the Sun. The quantities x, z, v, and $-C/2$ are the coordinate along the Sun–asteroid line, the vertical coordinate, the speed, and the orbital energy, respectively—all measured in the rotating asteroid–centered reference frame. This expression is accurate to first order in r/R (cf. Eq. (1)).

Next, we convert the asteroid-centered Jacobi integral into orbital elements relative to the asteroid. The first and last terms are simple to convert and yield a result which is only slightly different from Eq. (2),

$$C = \frac{GM}{a} + 2nn_\odot a^2(1 - e^2)^{1/2} \cos(i) + n_\odot^2(3x^2 - r^2), \qquad (4)$$

where $n = (GM/a^3)^{1/2}$ is the mean motion of the satellite around the asteroid, and a, e, i are the semimajor axis, eccentricity, and inclination of the circumasteroidal orbit. The first two terms of Eq. (4) are much larger than the final term for strongly bound orbits but inclusion of the

final term, which contains the solar tidal perturbations on circumasteroidal orbits, extends the zone of validity of the Tisserand Constant to more distant orbits. Unfortunately, the solar tidal term is more difficult to transform into orbital elements; its conversion yields an expression with 12 terms which not only are functions of the semimajor axis a, eccentricity e, and inclination i, as Tisserand's Constant (Eq. (2)) is, but also are functions of the longitudes of the ascending node Ω, pericenter ϖ, and the satellite l as well (six variables in all). To reduce the complexity of this result, we make two simplifying assumptions. First, we limit our study to planar orbits, which eliminates the dependence on i and Ω, and second, we average our expression over one circuit of the satellite around the asteroid, which eliminates the dependence on l. The result is the Generalized Tisserand Constant:

$$C = \frac{GM}{a} \pm 2nn_\odot a^2(1-e^2)^{1/2} + \frac{a^2 n_\odot^2}{2} + \frac{3a^2e^2n_\odot^2}{4}[1 + 5\cos(2\phi_\odot)], \quad (5)$$

where the plus sign corresponds to prograde orbits ($i = 0$) and the minus sign to retrograde orbits ($i = 180°$), and $\phi_\odot$ is the angle between the Sun and the orbit's pericenter as seen from the asteroid.

When orbit-averaging, however, we make the implicit assumption that the changes to a Keplerian orbit due to perturbations are small over one orbital period. This approximation is the most restrictive of all those made so far; it introduces errors which are greatest for orbits most distant from the asteroid (where the solar gravity is a large perturbation). In addition, orbit-averaging results in a purely secular expression—mean motion resonances between the satellite and asteroid orbital periods, which are important for some distant orbits (e.g. Jupiter's Sinope, Saha and Tremaine 1993), are ignored by our method. Finally, Eq. (5) need not remain constant all along an orbit, only its average is conserved from one orbit to the next. Since the orbit-averaging procedure also yields the result a = const (e.g. Hamilton 1993), our two approximations reduce the number of variables from six to only two: e and $\phi_\odot$. Combining the constants C, GM/a, and $a^2n_\odot^2/2$ into a single constant H and dividing through by $2nn_\odot a^2$, we finally obtain:

$$H = \pm(1-e^2)^{1/2} + \frac{3n_\odot e^2}{8n}[1 + 5\cos(2\phi_\odot)], \quad (6)$$

where again the plus sign corresponds to prograde orbits and the minus sign to retrograde orbits. The prograde version of this expression was first derived by Hamilton and Krivov (1996) using another method. The present derivation is particularly enlightening, however, because (i) it connects Eq. (6) to the well-known Jacobi integral of the circular restricted three-body problem, and (ii) it demonstrates unambiguously that Eq. (6) may be generalized to three dimensions.

The three-dimensional version of Eq. (6) can be further generalized by the inclusion of additional time-independent forces that can be derived from potentials including planetary oblateness and solar radiation pressure (Hamilton and Krivov 1996). Electromagnetic forces on a charged ring particle orbiting in a spinning dipolar magnetic field cannot be included for three-dimensional orbits but, for planar orbits, Hamilton and Krivov (1996) found an "effective" electromagnetic energy which, when added to Eq. (6), reproduces the correct equations of motion.

3. PROGRADE AND RETROGRADE ORBITS

3.1. *Distant Orbits*

The validity of the Generalized Tisserand Constant may be tested by performing numerical integrations of asteroidal satellites and monitoring the constant H as calculated from Eq. (6). We use a simple Bulirsch-Stoer routine and numerically solve Newton's $F = ma$ in a frame centered on the asteroid. As expected, H is well conserved for orbits close to the asteroid (which are nearly Keplerian). For more distant orbits, solar perturbations are stronger, orbit-averaging yields poorer results, and H is less well conserved. Nevertheless, even for very distant orbits H remains nearly constant and is still a useful quantity. We demonstrate this with several example orbits started with $a = 0.3820r_H$ (this corresponds to $\sim 64(R/1\ AU)(\rho/2.0\ \mathrm{g\ cm^{-3}})^{1/3}$ asteroid radii or about 1.5 times the lunar distance for Earth-centered orbits), eccentricities between 0.0 and 0.8, and $\phi_\odot = 0$. Here $r_H = (M/3M_\odot)^{1/3}R$ is the radius of the Hill sphere. The orbits, which are plotted in Fig. 1, are not far from the numerically determined prograde stability limit at $0.49r_H$ (Hamilton and Burns 1991).

Rather than showing plots of H versus time for the orbits of Fig. 1, we take advantage of the fact that H can be easily plotted as a function of the two variables e and $\phi_\odot$. In Fig. 2, we show contours of constant H for orbits with $a = 0.3820r_H$ as calculated from Eq. (6). In addition, we translate the (x, y) pairs of Fig. 1 into $(e, \phi_\odot)$ pairs and overplot them on each panel of Fig. 2. In this way, we can compare numerical integrations directly to theory. The numerically determined orbits of Fig. 2 are elongated as predicted by the contours, but have nonzero width due to variations of H over one orbital period. This indicates that the orbit-averaging approximation is not especially good for such distant orbits. Furthermore, the orbits with eccentricities 0.7 and 0.8 are more elongated than predicted which indicates that our method is less accurate for these highly eccentric orbits. Orbits with large eccentricities reach

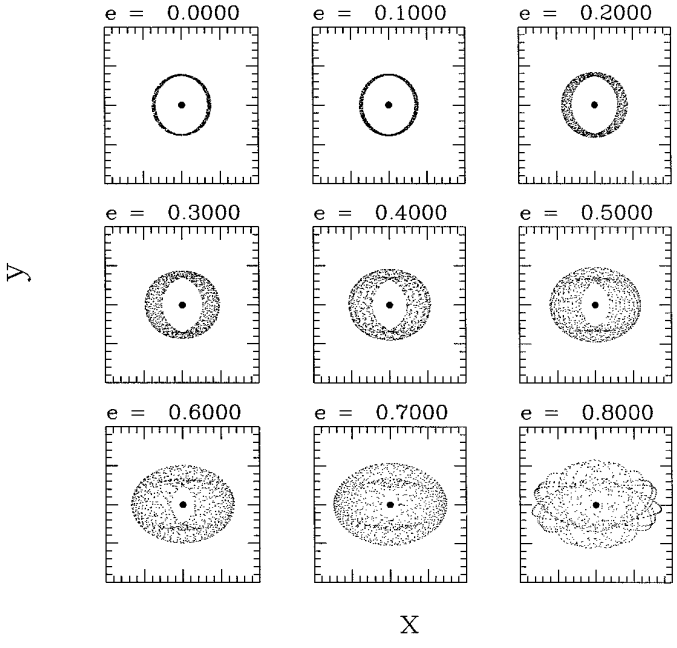

FIG. 1. Nine prograde orbits started at pericenter with $a = 0.3820 r_H$, eccentricities between 0.0 and 0.8, and $\phi_\odot = 0$; here $r_H = (M/3M_\odot)^{1/3} R$ is the Hill radius. The orbits are plotted in a rotating frame centered on the asteroid (solid circle, not to scale), so the Sun is always located along the positive x-axis. The length and width of each box is $1.0 r_H$. Note that the zones swept out by the orbits are elongated along the Sun–asteroid line.

greater distances from the asteroid where the larger solar perturbations cause our averaging method to be less valid. Nevertheless, it is a triumph for the method that it successfully predicts the shape and orientation of these distant orbits.

From the level curves of Fig. 2, we can also predict the shape and orientation of the orbits in space (cf. Fig. 1). Each orbit reaches its maximum eccentricity, and also its most distant and closest points to the asteroid, when $\phi_\odot = 0$ or $\phi_\odot = \pi$. Thus the level curves of Fig. 2 correctly predict that orbits will be stretched toward and away from the Sun in Fig. 1. The level curves also imply that the entire family of prograde orbits with $a = 0.3820 r_H$ will be elongated along the Sun–asteroid line since any initial condition in the $(e, \phi_\odot)$ plane should closely follow one of the oval curves in the clockwise direction (see Fig. 2). This is a powerful statement: Fig. 2 predicts the shape of all orbits with $a = 0.3820 r_H$, regardless of the starting eccentricity e, solar angle $\phi_\odot$, and position along the elliptical orbit l.

Finally, while Eq. (6) gives the exact shape of the level curves of Fig. 2, it provides no information about the time it takes a satellite to complete one circuit around a given level curve. For weakly perturbed orbits, however, the angle between the Sun and orbital pericenter, $\phi_\odot$, varies primarily due to the motion of the Sun. Hence it takes about one asteroidal year for a satellite to travel around each of the level curves. Since the eccentricity is maximum at $\phi_\odot = 0$ and $\phi_\odot = \pi$ (Fig. 2), the eccentricity varies with a period of one half an asteroid year. This result is in agreement with perturbation theory, e.g. Goldreich *et al.* (1989), and with numerical integrations, e.g. Hamilton and Burns (1991), Benner and McKinnon (1995a).

Figures 3 and 4 are the retrograde equivalents of Figs. 1 and 2. Although the initial satellite–asteroid separation is the same in all four figures, several interesting differences between the prograde and retrograde plots are immediately apparent. First, the retrograde orbits and curves of constant H are extended perpendicular to the Sun-asteroid line rather than parallel to it. The different orientation of the prograde and retrograde level curves of H follows from the change of sign in Eq. (6), and Fig. 4 shows that this perpendicular extension is a general property of the entire family of retrograde orbits with $a = 0.3820 r_H$. Furthermore, a careful inspection of Figs. 2 and 4 shows that the level curves are less elongated for retrograde orbits than for prograde ones; this property is also apparent in the

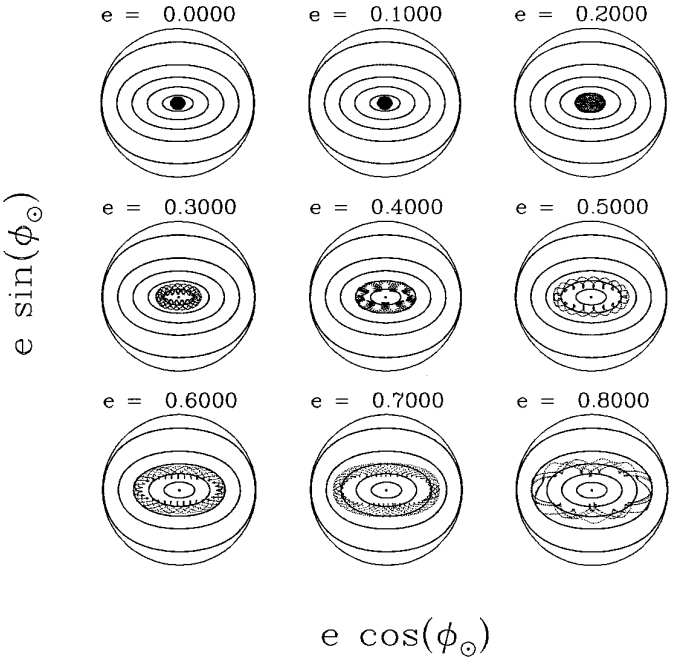

FIG. 2. Lines of constant H for prograde orbits from Eq. (6) (oval curves) plotted in polar coordinates $h = e\cos(\phi_\odot)$ and $k = e\sin(\phi_\odot)$ for the conditions of Fig. 1. Curves correspond to initial conditions $e = 0.0$, 0.2, 0.4, 0.6, 0.8, and 1.0 with $\phi_\odot = 0$—the outer circles indicate $e = 1$. For each panel, the orbit from the corresponding panel of Fig. 1 was translated into $(e, \phi_\odot)$ coordinates and plotted as points over the lines of constant H. The agreement between theory (ovals) and the numerically calculated orbits is good, but not perfect. Nevertheless, in all cases the curves are broadest along the horizontal axis which indicates the orbits are most eccentric when $\phi_\odot = 0$ or $\phi_\odot = \pi$; i.e., these orbits extend furthest from the asteroid in the solar and antisolar directions in agreement with Fig. 1.

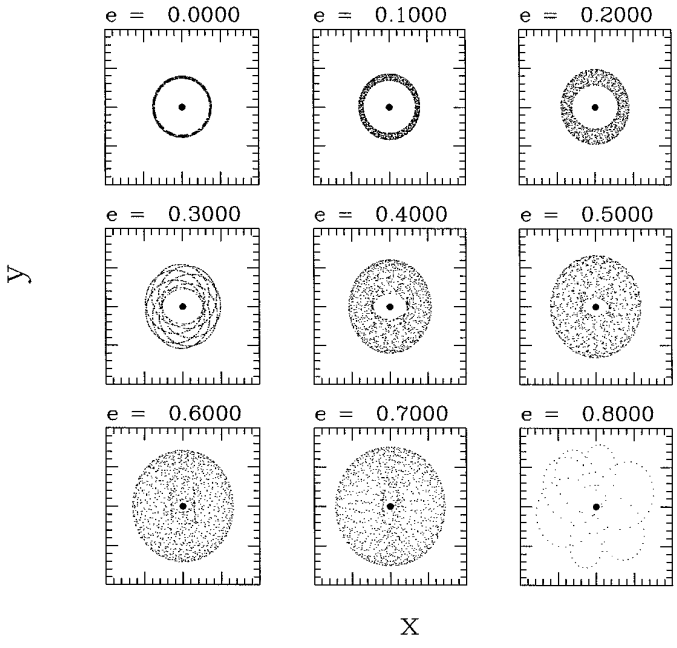

FIG. 3. Nine retrograde orbits started at pericenter with $a = 0.3820 r_H$, eccentricities between 0.0 and 0.8, and $\phi_\odot = 0$. As in Fig. 1, the orbits are plotted in rotating coordinates with the Sun along the positive x-axis, the asteroid is marked with a solid circle, and the size of the box is $1.0 r_H$. Note that, in contrast to Fig. 1, the retrograde orbits are most extended perpendicular to the Sun–asteroid line. The particle in the final graph collided with the asteroid after a short time.

actual orbits displayed in Figs. 1 and 3. This shape difference between prograde and retrograde orbits stems from the interplay between the $\phi_\odot$-dependent and the $\phi_\odot$-independent parts of the second term of Eq. (6); in the vertical directions of Figs. 2 and 4, these terms compete, while in the horizontal directions they reinforce one another.

3.2. *Very Distant Orbits*

All of these differences between prograde and retrograde orbits can be more clearly seen when the initial starting distance from the asteroid is varied. Figures 5 and 6 show prograde orbits similar to Figs. 1 and 2, except that we vary the orbital size rather than the eccentricity from panel to panel. All prograde orbits in Fig. 5 are started on initially circular paths; these orbits become progressively more perturbed as the initial distance is increased until escape from the asteroid inevitably occurs. Low-energy escape from circumasteroidal space always occurs near one of the Lagrange points located along the Sun–asteroid line at $a = r_H$ (Hamilton and Burns 1991); in Fig. 5, the four escape orbits all slip past L_1, the Lagrange point between the asteroid and the Sun, on their way to heliocentric space.

The phase curves of Fig. 6, by contrast, predict that all prograde orbits remain bound since the level curves all close. In fact, Eq. (6) can never directly predict escape because our orbit-averaged approximation assumes bound, nearly Keplerian orbits. Using Eq. (6) to study the bound–escape transition pushes the theory beyond its design specifications but, surprisingly, the level curves of Fig. 6 still provide useful information for these very distant orbits. For instance, note the gradual transformation of phase space with increasing distance in Fig. 6. The curves start out nearly circular in the upper left graph, indicating that the orbital eccentricities of not-so-distant prograde orbits do not change much. Level curves for more distant orbits are increasingly flattened along the Sun–asteroid line and finally, for orbits distant enough to escape, the prograde phase space begins to show a figure-eight topology. These results predict that all bound prograde orbits, regardless of their size, are extended along the Sun–asteroid line with the distortion increasing for larger orbits. Furthermore, when escape does occur, it occurs along the Sun–asteroid line where tidal forces are greatest and where Eq. (6) predicts that prograde orbits are most elongated.

The change in topology of the phase portraits in Fig. 6 is also quite interesting. The oval topology for near-asteroid

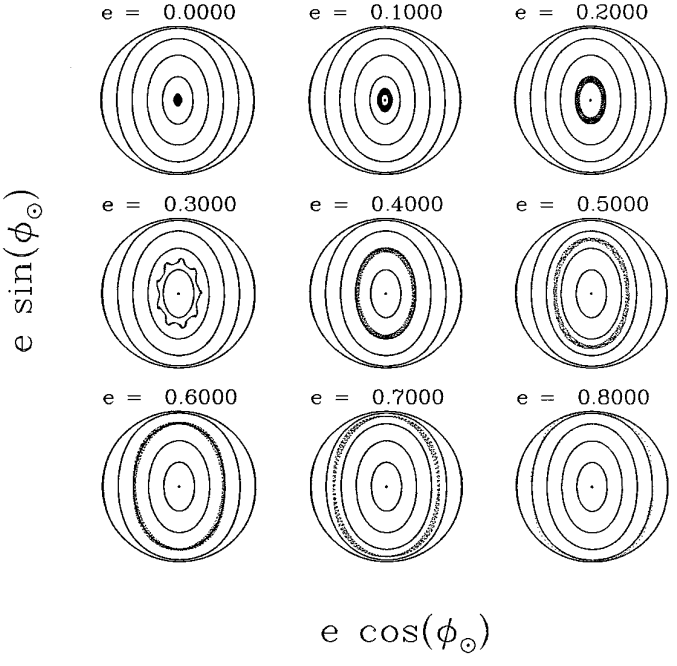

FIG. 4. Lines of constant H (selected as in Fig. 2) for retrograde orbits from Eq. (6) (oval curves) plotted in polar coordinates $h = e\cos(\phi_\odot)$ and $k = e\sin(\phi_\odot)$ for the conditions of Fig. 3. The orbits were overplotted in the same manner as in Fig. 2. The agreement between theory (ovals) and the orbits is significantly better than in Fig. 2, but differences are still noticeable. In all cases the curves are broadest along the vertical axis which indicates the orbits are most eccentric when $\phi_\odot = \pi/2$ or $\phi_\odot = 3\pi/2$; these orbits extend furthest from the asteroid in directions perpendicular to the Sun–asteroid line in agreement with Fig. 3.

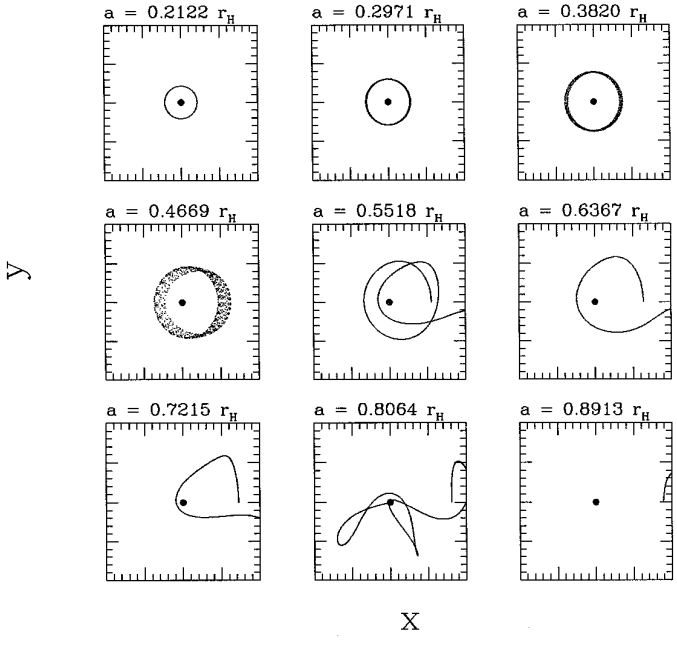

FIG. 5. Nine different-sized prograde orbits started with $e = 0.0$ from the positive x-axis. Coordinates and symbols are as in Fig. 1. In the first four panels, the satellite is bound, in panel 8 it crashes into the asteroid, and in the remaining panels it escapes. Note that bound orbits are stretched in along the Sun–asteroid line (x-axis) and that escape always occurs along this line.

orbits has an equilibrium point at $e = 0$, which corresponds to an unperturbed circular orbit (first graph in Figs. 5 and 6). Taken literally, Eq. (6) predicts that orbits with $e = 0$ should be unperturbed; in reality, short-period oscillations ignored in the orbit-averaging process cause orbits to evolve somewhat, but eccentricities do remain small as predicted (top three graphs of Figs. 5 and 6). The figure-eight topology, by contrast, has three equilibrium points—2 maxima and a saddle at $e = 0$ (Hamilton and Krivov 1996). Orbits starting with $e = 0$ are not stable, but rather evolve rapidly so that they are extended along the Sun–asteroid line; i.e. these orbits change from relatively safe circular orbits to elongated ones which are subject to strong destabilizing tidal perturbations. It is perhaps not surprising that orbits begin to escape at just about the point where the single equilibrium point at $e = 0$ bifurcates into three. By considering the derivatives of Eq. (6), we find that the prograde change of topology occurs at $A \equiv 3n_\odot/4n = 1/6$ (Hamilton and Krivov 1996), which can be written as $a = 0.53r_H$, while numerical simulations show that initially circular orbits escape when launched at distances outside about $0.49r_H$ (Hamilton and Burns 1991).

We should be very careful to avoid overinterpreting the predictions of the figure-eight phase space—after all, this topology occurs only for very distant orbits which are not well governed by Eq. (6). Nevertheless, there are several indications that the underlying figure-eight topology is a good approximation to reality. First, if we interpret the predictions of the bottom row of Fig. 6's graphs literally, initially circular orbits should increase their eccentricities to the point where impacts with the asteroid are possible. While most distant orbits are stripped away from the asteroid before an impact occurs, the orbit in the eighth graph of Fig. 5 does intersect the asteroid as predicted; in fact, this hypothetical satellite strikes the asteroid from roughly the anti-Sun direction, one of the two possibilities predicted by Fig. 6. Second, consider the fourth panel of Figs. 5 and 6 which shows an interesting orbit which always keeps its pericenter away from the Sun. This type of librating orbit is exactly what is predicted to exist in the left-hand lobe of one of the figure-eights of Fig. 6, although it appears slightly earlier than our theory predicts. Support for this interpretation comes from work by Hénon (1969) who studied periodic orbits in Hill's problem. Working with prograde orbits, Hénon (1969) found a bifurcation of a stable nearly-circular periodic orbit (his critical orbit $g1$) into a symmetric pair of stable elongated periodic orbits (members of his family g') and an unstable periodic orbit (a member of his family g). We identify our topology change with Hénon's bifurcation of simple periodic orbits

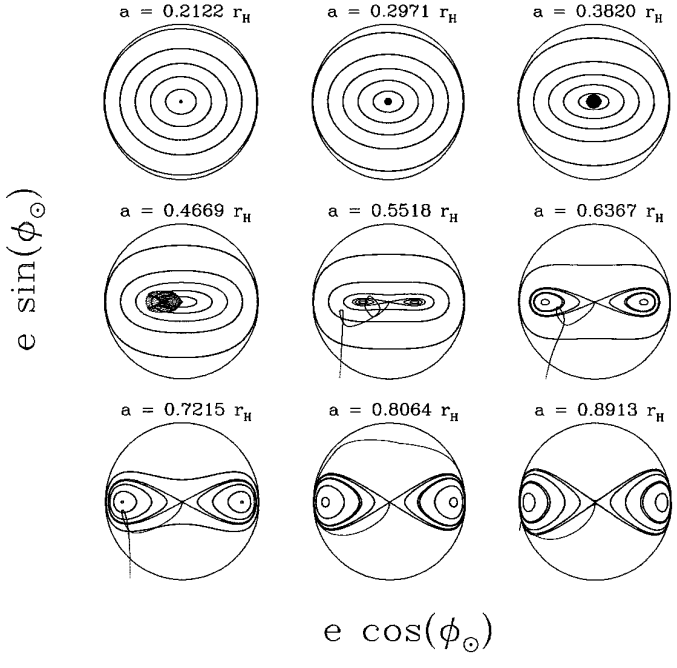

FIG. 6. Phase plots: lines of constant H for the prograde orbits of Fig. 5 (cf. Fig. 2). Curves correspond to initial conditions $e = 0.0$, 0.2, 0.4, 0.6, 0.8, and 1.0 with $\phi_\odot = 0$ and 180°. Note the change in topology between the fourth and fifth graphs, roughly coincident with where escape first occurs in Fig. 5. In each panel, the initially circular orbit from Fig. 5 is converted into $h = e\cos(\phi_\odot)$ and $k = e\sin(\phi_\odot)$ coordinates and overplotted.

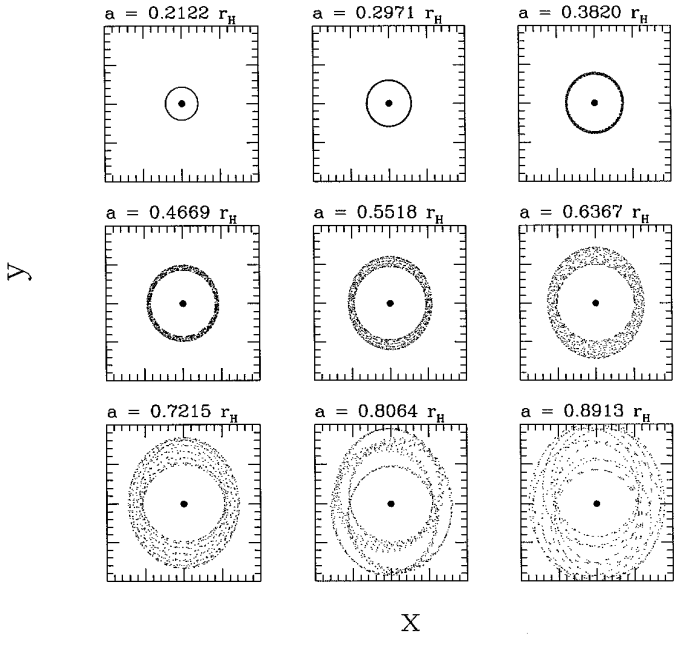

FIG. 7. Nine different-sized retrograde orbits started with $e = 0.0$ from the positive x-axis. Coordinates and symbols are as in Fig. 1, and starting distances are as in Fig. 5. All orbits are bound and extended perpendicular to the Sun–asteroid line. Note that this extension is more pronounced for larger orbits.

(in our approximation, all orbits are simple periodic!). Hénon's bifurcation occurs at $a = 0.45r_H$, which agrees well with our numerical results for the librating orbit of Figs. 5 and 6. The discrepancy between this value and our prediction of $0.53r_H$ illustrates the errors inherent in applying our orbit-averaged approach to distant orbits, and is the price that one pays for simplicity!

Figure 7 shows initially circular retrograde orbits started at the same distances as the prograde orbits in Fig. 5; Fig. 8 is the phase-portrait counterpart. All of the retrograde orbits in Fig. 7 are bound and stretched perpendicular to the Sun–asteroid line as predicted by the contours of Fig. 8. Furthermore, as with prograde orbits, the distortions increase with distance from the asteroid until finally retrograde orbits become perturbed enough to escape at about $a = r_H$. Thus Fig. 8 predicts that all retrograde orbits, regardless of a, e, $\phi_\odot$, and l, are elongated perpendicular to the Sun–asteroid line. Increasing distortions in these directions are consistent with the limiting epicyclic motion in the rotating frame: i.e. for extremely distant retrograde orbits, the asteroid's gravity is unimportant and motion in the rotating frame occurs along a 2:1 ellipse centered on the asteroid and elongated perpendicular to the Sun–asteroid line (Hamilton and Burns 1991). The 2:1 ellipse is a member of a retrograde family of periodic orbits, all of which are elongated perpendicular to the Sun–asteroid line and all of which are stable (Hénon 1969). As with prograde orbits, we calculate the point at which the retrograde change of topology occurs ($A = 1/4$ or $a = 0.69r_H$) and compare it to the numerically determined escape distance of $a = r_H$. The discrepancy between these values is large, and it appears that the figure-eight topology is not a good indicator of instability for retrograde orbits. In fact, Hénon (1969) finds that his retrograde family of periodic orbits, family f, experiences no bifurcation, hence it is likely that the topology change that we find is an artifact of the averaging process. These conclusions are supported by the two largest orbits of Figs. 7 and 8, which do not extend as far from the asteroid as their level curves predict.

Our secular orbit-averaged theory predicts that all prograde orbits are elongated along the Sun–asteroid line while all retrograde orbits are extended in the perpendicular directions. This conclusion is consistent with the fact that the majority of simple periodic orbits studied by Hénon (1969) are stable when they are elongated in the directions that we predict in this work. In addition, Hénon's unstable periodic orbits are almost alway elongated in directions opposite to our predictions. In comparing Figs. 5–8, note that, for each distance, the prograde curves are more elongated than their retrograde counterparts as we noticed for the $a = 0.3820r_H$ examples in Figs. 1–4. This too, is a general property of distant orbits. Another difference between prograde and retrograde is that while the pre-

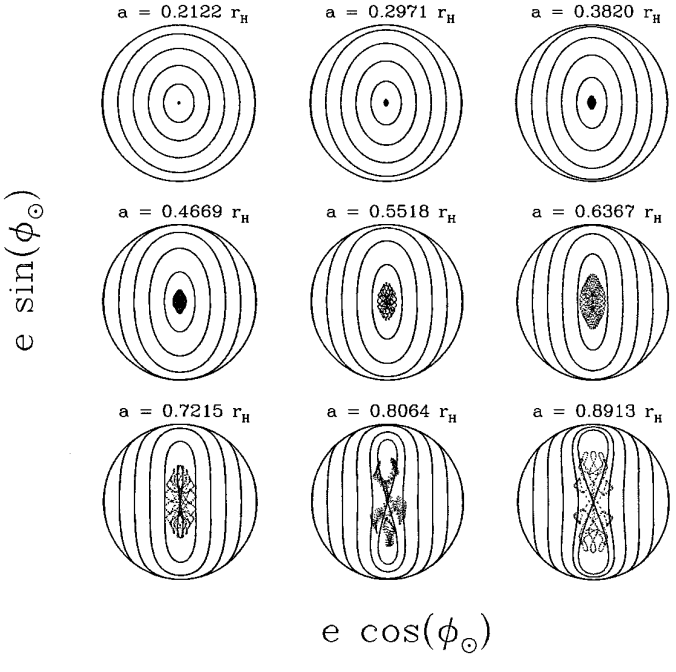

FIG. 8. Phase plots: lines of constant H for the retrograde orbits of Fig. 7 (cf. Fig. 4). Note the change in topology between the sixth and seventh graphs. In each panel, the initially circular orbit from Fig. 7 is converted into $h = e\cos(\phi_\odot)$ and $k = e\sin(\phi_\odot)$ coordinates and overplotted.

dicted topology of phase space changes from ovals to figure-eights for both types of orbits, the transformation occurs closer to the asteroid for prograde orbits than for retrograde ones.

These differences between prograde and retrograde orbits, all of which follow from the Generalized Tisserand Constant, support the notion that retrograde orbits should be more stable that prograde ones. Prograde orbits are elongated in the ''dangerous'' toward-Sun and away-from-Sun directions where the solar tidal forces are strongest, while retrograde orbits are extended in the perpendicular directions. In addition, the change in topology from ovals to figure-eights occurs earlier for prograde than for retrograde orbits. If we use topology change as an approximate criterion for escape, we obtain analytic results (stability for initially circular prograde orbits with $a < 0.53r_H$ and for initially circular retrograde orbits with $a < 0.69r_H$) which, while not in impressive agreement with numerical results, are superior to all others attained to date. In fact, these results are the only ones based on the Jacobi Constant that correctly predict that prograde orbits are less stable than retrograde ones. There are several caveats, however. Our naive change-of-topology criterion ignores the orientation of the figure-eight in phase space and includes errors introduced in the averaging process. It also assumes that the change in the phase space topology corresponds to a real change in orbital dynamics, which although true for prograde orbits, appears not to be the case for retrograde ones. For these reasons, and because the effects of the Coriolis acceleration are not include in the Generalized Tisserand Constant as discussed below, the stability limits predicted by this method should not be taken too seriously.

Another major difference between prograde and retrograde orbits is that, at a given distance, the retrograde orbits (Figs. 4 and 8) clearly fit the predictions of Eq. (6) much better than do the prograde orbits (Figs. 2 and 6). This indicates that our assumptions, in particular the orbit-averaged approximation, are better for retrograde orbits. Since the Generalized Tisserand Constant predicts that all orbits are bound, its validity must break down before satellites can actually escape; hence prograde orbits are able to escape earlier than retrograde ones. This difference cannot be understood with the Generalized Tisserand Constant; it follows rather from the Coriolis acceleration in the rotating frame as pointed out by Hamilton and Burns (1991). The effects of the Coriolis acceleration are not included in Eq. (6), which is the energy integral in a frame rotating with the mean motion of the asteroid around the Sun. Since the Coriolis acceleration is always perpendicular to the satellite's velocity vector, it cannot affect the energy integral. The Coriolis acceleration points inward for retrograde orbits and outward for prograde orbits (Hamilton and Burns 1991) which tends to stabilize and destabilize these orbits, respectively. In Figs. 2, 4, 6 and 8, the Coriolis acceleration causes satellites to move along the curves of constant H in such a way that retrograde satellites complete one cycle faster than prograde orbits do. This gives prograde orbits more time to built up greater deviations from the prediction of Eq. (6) than retrograde orbits as seen in Figs. 2, 4, 6, and 8. Hence the Coriolis acceleration, like the Generalized Tisserand Constant, causes prograde orbits to be less stable than retrograde ones (Hamilton and Burns 1991). It is the omission of Coriolis effects that limits the accuracy of all escape criteria derived from the Jacobi Constant, including our change-of-topology criterion discussed in the last paragraph.

4. SUMMARY

In this short paper, we have derived an accurate asteroid-centered (or planet-centered) version of Tisserand's Constant and applied it to planar prograde and retrograde orbits around asteroids moving on circular paths around the Sun. Our method is most applicable to distant orbits which are far enough from the asteroid that the effects of its asymmetric gravity field may be ignored, but close enough that the orbits are only weakly perturbed by solar gravity. The method also proves to be a useful guide for the more distant strongly perturbed orbits studied here. Simple analytical arguments based on the Generalized Tisserand Constant show that all prograde orbits are extended along the Sun-asteroid line and that all retrograde orbits are elongated at right angles to this line, with the magnitude of the distortion increasing for more distant orbits. More careful reasoning, using the Generalized Tisserand Constant, knowledge of the form of the tidal acceleration field, and of the direction of the Coriolis acceleration (whose effects are not included in Eq. (6)) shows that retrograde orbits are more stable that prograde ones.

Our approach can be extended to three dimensions, but the resulting expression is somewhat unwieldy. Nevertheless, a three-dimensional version of Eq. (6) may provide explanations for additional properties of distant orbits, such as the propensity for objects on highly inclined orbits to strike the central asteroid (Hamilton and Burns 1991, 1992). A spectacular example of the instability of highly inclined orbits is given by Lidov (1961, 1963) who showed that if the Moon had a circular $i = 90°$ orbit, it would strike the Earth in just over six years! Comet Shoemaker–Levy 9, a temporary highly inclined satellite of Jupiter which struck the planet in 1994, provides another dramatic example (Benner and McKinnon 1995b). As with the planar prograde and retrograde orbits studied here, however, the most interesting effects occur when the orbit-averaging approximation begins to break down; in such cases the Generalized Tisserand Constant must be applied with caution.

ACKNOWLEDGMENTS

We thank Prasenjit Saha and Dan Scheeres for their detailed and helpful reviews of this work.

REFERENCES

Benner, L. A. M., and W. B. McKinnon 1995a. Orbital behavior of captured satellites: The effect of solar gravity on Triton's postcapture orbit. *Icarus* **114,** 1–20.

Benner, L. A. M., and W. B. McKinnon 1995b. On the orbital evolution and origin of Comet Shoemaker–Levy 9. *Icarus* **118,** 155–168.

Brown, E. W., and C. A. Shook 1933. *Planetary Theory.* Cambridge Univ. Press, Cambridge, UK.

Chauvineau, B., and F. Mignard 1990a. Dynamics of binary asteroids I–Hill's case. *Icarus* **83,** 360–381.

Chauvineau, B., and F. Mignard 1990b. Dynamics of binary asteroids II–Jovian perturbations. *Icarus* **87,** 377–390.

Danby, J. M. A. 1988. *Fundamentals of Celestial Mechanics,* 2nd ed. Willmann–Bell, Richmond, VA.

Geissler, P., J.-M. Petit, D. Durda, R. Greenberg, W. Bottke, M. Nolan, and J. Moore 1995. Erosion and ejecta reaccretion on 243 Ida and its moon. *Icarus* **120,** 140–157.

Goldreich, P., N. Murray, P. Y. Longaretti, and D. Banfield 1989. Neptune's story. *Science,* **245,** 500–504.

Hamilton, D. P. 1993. Motion of dust in a planetary magnetosphere: Orbit-averaged equations for oblateness, electromagnetic, and radiation forces with application to Saturn's E ring. *Icarus* **101,** 244–264; Erratum. *Icarus* **103**, 161.

Hamilton, D. P., and J. A. Burns 1991. Orbital stability zones about asteroids. *Icarus* **92,** 118–131.

Hamilton, D. P., and J. A. Burns 1992. Orbital stability zones about asteroids II. The destabilizing effects of eccentric orbits and of solar radiation. *Icarus* **96,** 43–64.

Hamilton, D. P., and A. V. Krivov 1996. Circumplanetary dust dynamics: Effects of solar gravity, radiation pressure, planetary oblateness, and electromagnetism. *Icarus* **123,** 503–523.

Hénon, M. 1969. Numerical exploration of the restricted problem, V. *Astron. Astrophys.* **1,** 223–238.

Hénon, M., and J. M. Petit 1986. Series expansions for encounter-type solutions of Hill's problem. *Celest. Mech.* **38,** 67–100.

Huang, T.-Y., and K. A. Innanen 1983. The gravitational escape/capture of planetary satellites. *Astron. J.* **88,** 1537–1548.

Innanen, K. A. 1979. The limiting radii of direct and retrograde satellite orbits, with applications to the solar system and to stellar systems. *Astron. J.* **84,** 960–963.

King, I. 1962. The structure of star clusters. I. An empirical density law. *Astron. J.* **67,** 471–485.

Lidov, M. L. 1961. Evolution of orbits of artificial planetary satellites perturbed by gravity of external bodies. In *Artificial Earth Satellites,* Issue 8. [In Russian]

Lidov, M. L. 1963. On the approximate analysis of orbital evolution of artificial satellites. In *Problems of Motion of Artificial Celestial Bodies.* Academy of Sciences of USSR, Moscow. [in Russian]

Markellos, V. V., and A. E. Roy 1981. Hill stability of satellite orbits. *Celest. Mech.* **23,** 269–275.

Murray, C. D., and D. Harper 1993. *Expansion of the Planetary Disturbing Function to Eighth Order in the Individual Orbital Elements,* QMW Math Notes No. 15. Queen Mary and Westfield College, London.

Saha, P., and S. Tremaine 1993. The orbits of the retrograde jovian satellites. *Icarus* **106,** 549–562.

Scheeres, D. J. 1994. Dynamics about uniformly rotating tri-axial ellipsoids. *Icarus* **110,** 225–238.

Scheeres, D. J., S. J. Ostro, R. S. Hudson, and R. A. Werner 1996. Orbits close to Asteroid 4769 Castalia, *Icarus* **121,** 67–87.

Szebehely, V. 1978. Stability of artificial and natural satellites. *Celest. Mech.* **18,** 383–389.

Zhang, S. P., and K. A. Innanen 1988. The stable region of satellites of large asteroids. *Icarus* **75,** 105–112.